5. Effects of Charge-up

In an early stage of testing, we recognized that the sensors are easier to charge up compared to ISL/L00 sensors. Typically 30-40 central strips were affected by charge-up, showing smaller resistances and non-uniform coupling capacitors, as plotted in Fig. 10a. From the location and spread, we suspected that a vacuum tweezers used to pick up the sensor is causing the trouble. After eliminating use of tweezers, this effect turned to be hard to appear[1].

The charge-up mechanism can be explained that a thin *p*-type layer, an inversion layer, is created on the surface of *n*-type bulk by external static charges. This deteriorates the electrical isolation between strips, which was actually identified from our strip isolation test. This type inversion is easier to occur for <100> than for <111> because the positive charge trapped at the Si-SiO_2 interface and fixed oxide charge in SiO_2 layer are about one order abundant for <111>[2]. This explains qualitatively why we did not see charge-up for ISL/L00 sensors, which employ <111> wafers. It is important to note that HPK is checking the isolation for every strip. This insures that the isolation is degraded during handling.

The inversion layer could remain for a long time if there is no route for the charges to move. In our detector application, though, there are a couple of routes possible: (1) Al electrodes are connected to ASICs, (2) Signal currents are created by particles passing through, and (3) Positive ions are accumulated in oxide layer due to radiation. The

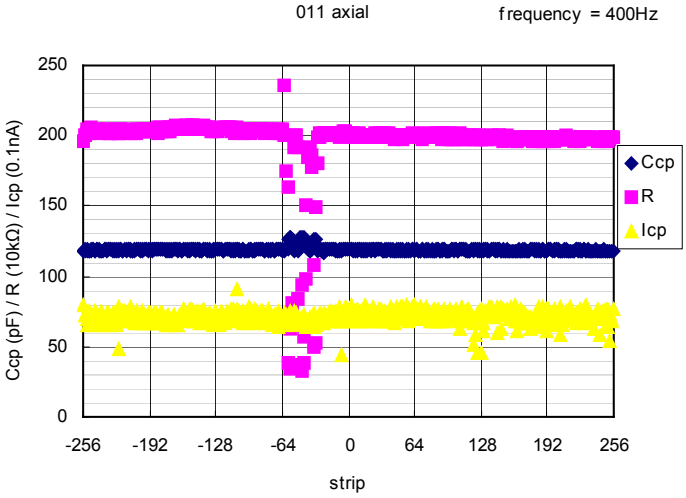

Fig.10a Example AC scan plot for a sensor with charge-up.

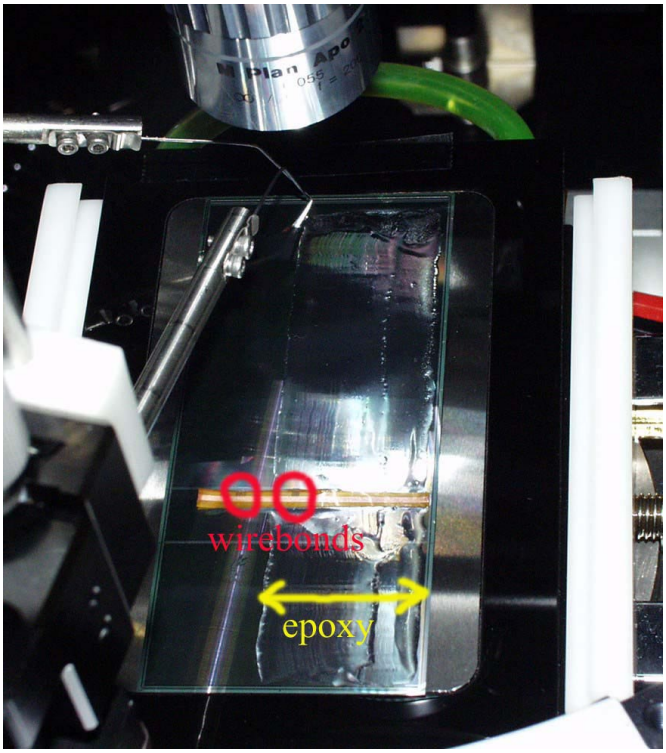

Fig. 10b Photo of the sensor used for charge-up study. Locations of wirebonds and epoxy are illustrated.

[1] Four consecutive sensors showed similar effects before we stop using tweezers. Recently, in order to carry out a study described here, we are back to use the same tweezers to intentionally charge a sensor up but failed. The sensitivity may depend how fresh the sensors are (surface charge condition), or environment such as humidity.

[2] See, for example, S. M. Sze, "Semiconductor Devices": John Wiley & Sons 1985.

positive ions (3) attract electrons at the oxide-silicon boundary, thus removing the inversion layer. Therefore the presence of inversion layer should not deteriorate the detector performance after the detector is in operation for a certain period.

We have investigated time constants for the inversion layer to disappear. The entire surface of a sensor was charged up by placing it on a stage which was severely charged by static electricity. In order to simulate the connections to ASICs, two clusters of 20 Al strips are wire-bonded to the bias-ring. Also we applied epoxy, Araldite 2011, on one half of the surface.

Figure 10b is a photo of the test sensor. Two groups (D100 to D80; 0 to U20) are grounded using AC pads for ASICs. The right side of the surface (ca. D40 to U255) is epoxied extending to full strip length. The thickness of the epoxy was not well under control, and there are two rows recognizable as in the photo. The amount of epoxy was too much exaggerated compared to our real case.

In the first part of the measurement, the AC scan was repeated while the sensor bias is kept at 200 V throughout the measurements. The leakage current was typically 0.2 µA. The evolution of the resistance is plotted in Fig. 10c. The initial was taken before the wire-bonds and gluing, showing almost all strips have 0.5 to 1.5 MΩ, which are substantially smaller than the nominal value of 1.7-1.9 MΩ. At T=0, when the sensor was biased first time since gluing/ wire-bonding which were done about 2 hrs before. The data shows that the resistances R are zero for wire-bonded strips (as they should be) and that R is smaller for strips in the glued region. A part of this could be attributed that the epoxy was not cured; epoxy curing time is 24 hrs. We also notice that the strips near the wire-bonded strips show quick recovery, which we expect. Then, in 50-60 hrs, almost all strips in the glued region recovered, but there is essentially no change in other region. This quicker recovery should be attributed that epoxy has finite conductivity.

In the second part of the measurement, which follows after T=61h, the sensor was illuminated with UV lamp and the AC scan was repeated. The leakage current while UV illuminated was 175

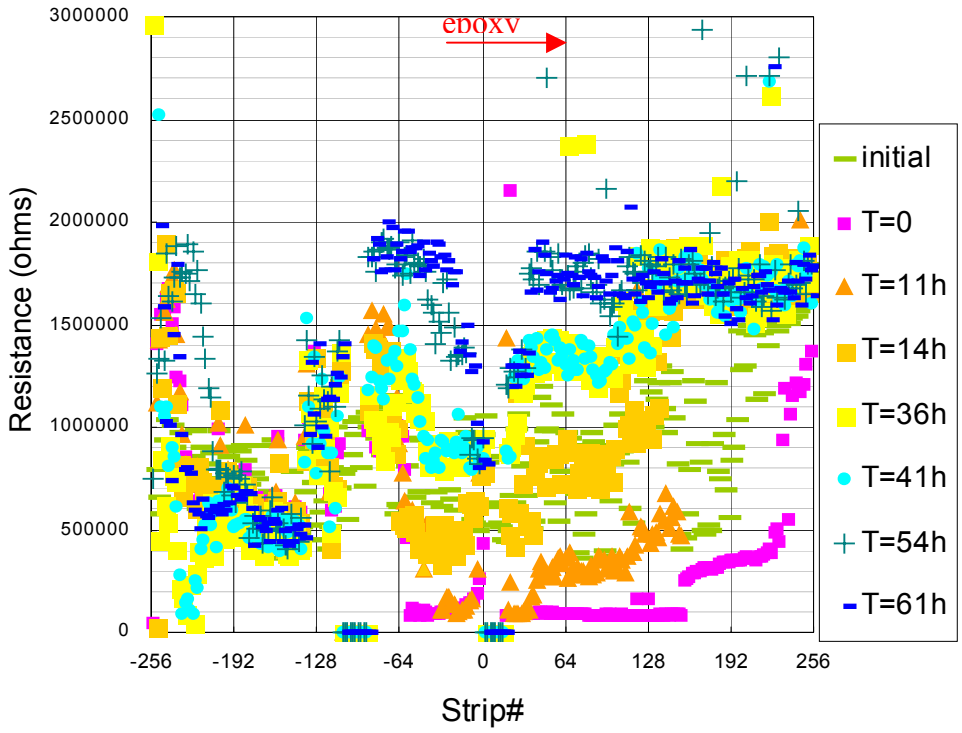

Fig. 10c Recovery of resistance values with time. The sensor is biased at 200 V. Ignore isolated data points due to poor probe contacts; the data were not re-measured.

μA at 200V (The UV was turned off during AC scans). The results are given in Fig. 10d. Though the probes were cleaned between 2nd and 3rd data taking, which introduced some effects other than UV, we can recognize that the strips near the grounded strips are recovering. Note also that the strips in the glued region are not much affected by UV. The UV illumination measurement was terminated at this stage: the charge up disappeared when the sensor was mistakenly removed from the stage.

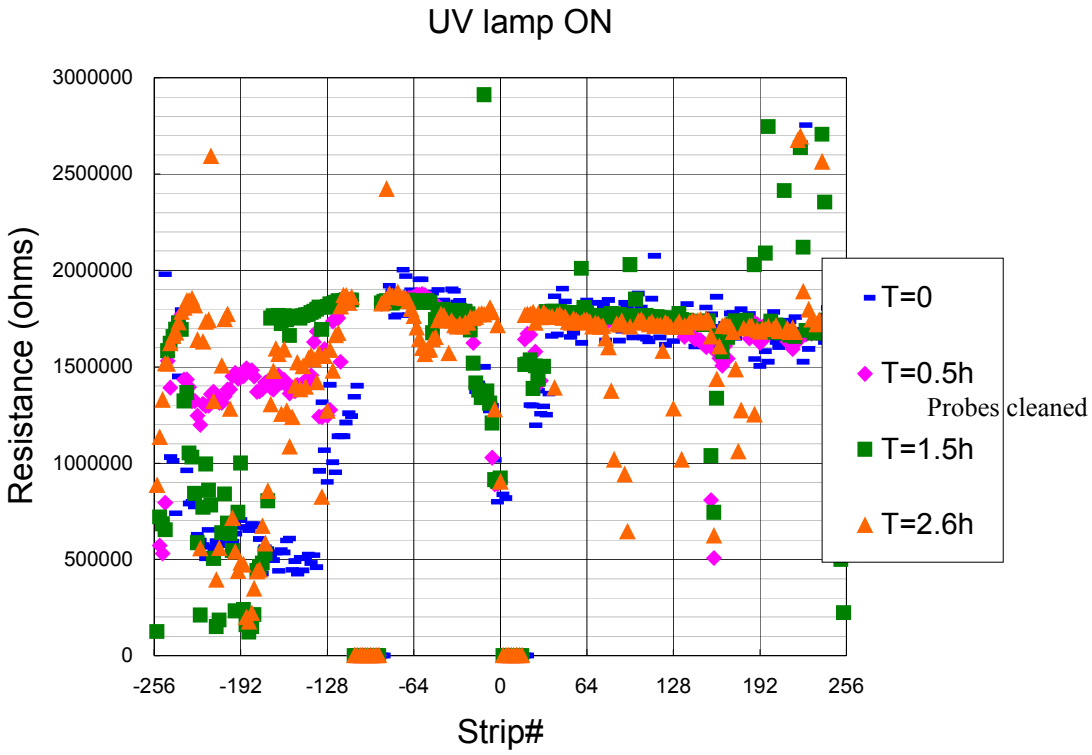

Fig. 10d Evolution of resistance values while the sensor is illuminated with UV. The time is the accumulated duration of UV illumination (The data T=0 is identical to the data T=61h in Fig. 10c). The sensor is biased at 200 V. Before taking data T=1.5h, the probes were cleaned and the bias was off. Ignore isolated data points due to poor probe contacts.

We summarize the present study. Avoid use of vacuum tweezers unless it is proven not to charge the sensor up. The charge-up effects, though, should diminish quickly if the sensors are wire-bonded. If the sensors are not wire-bonded, the surface charge could remain at least for days. Removal is accelerated if the sensor is illuminated by UV. Epoxy on the surface even helps remove the charge on the surface. Since epoxy degrades the surface isolation, use of epoxy has to be minimized. Otherwise, the sensor becomes easily affected by external conditions.

Note to add: We understand that the present study is not complete and wanted to carry out another measurement more systematically. As described in the previous footnote, though, we have not succeeded to charge a sensor up. Comparing the easiness of charge-up we encountered at earlier time, the sensor conditions must have changed. One of such changes could be that oxide layers have accumulated positive charges, which prevents the sensor from charge-up.

6. Performance of Neutron-Irradiated Sensors

The Hamamatsu sensors have been extensively studied on performance against radiation such as for LHC application. Our consensus is that HPK sensors are superior in all aspects and should be operational at least up to 2-3 x10^{14} n/cm^2. In order to verify this, we have irradiated 5 axial prototypes with neutrons at MNRC Irradiation Facility at UC Davis on September 27, 2002. The expected total doses were 1.4×10^{14} n/cm^2 for 3 sensors and 0.7×10^{14} n/cm^2 for 2 sensors. The two sensors irradiated to 0.7×10^{14} n/cm^2 were characterized at Tsukuba, which are reported here.

The sensors were cooled to extract characteristics which are not affected by the radiation induced large leakage current. Both sensors were glued on PC frames where fan-out readout traces are made. The back-plane, bias-ring, 10 consecutive AC pads and 10 consecutive DC pads were wire-bonded to these readout traces to allow us for testing described here. The sensor was placed in an environment chamber throughout the measurements. The measurements were carried out also in dry nitrogen environment, the results being essentially identical to those obtained in normal air.

6.1 Total Leakage Current

Fig. 11a shows I-V curves measured at temperatures ranging –30 to –10°C. First, we note that there is no breakdown up to 1000V we measured.

The measurements were carried out 45 days after irradiation. It is known that the leakage current of irradiated sensors will decrease (annealing) right after irradiation and later increase (anti-annealing). The damage constant α is expressed by $\alpha = \phi \cdot \Delta I / V$, where ϕ is the neutron fluence, ΔI is the increase in the total leakage current measured at full depletion voltage, and V is the volume of the sensor. Because of the features of annealing and temperature dependence of the leakage current, α is usually calculated after the initial annealing is completed and at 20°C.

Systematic measurements of the initial annealing are available such as from Rose Collaboration, which is shown in Fig. 11b. At room temperatures, the current decreases substantially within a month, approaching to an asymptotic damage constant of 3×10^{-17} A/cm.

Fig. 11c plots the leakage current at full depletion as a function of the temperature.

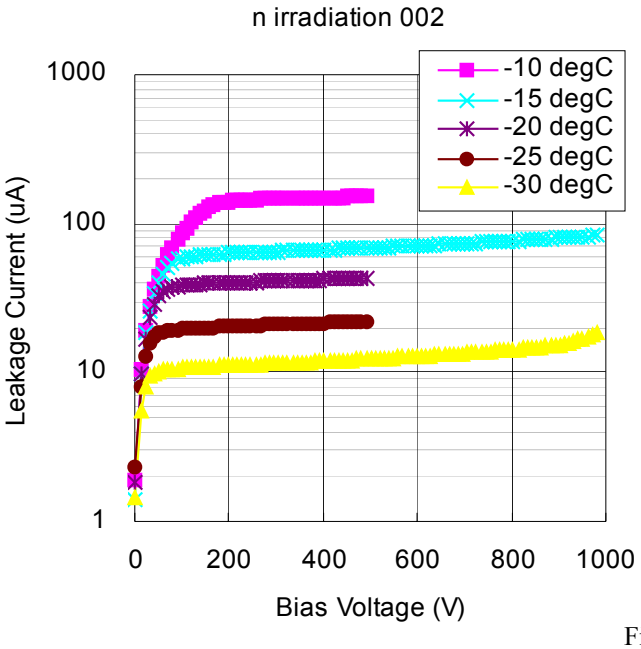

Fig. 11a I-V curves of irradiated sensor.

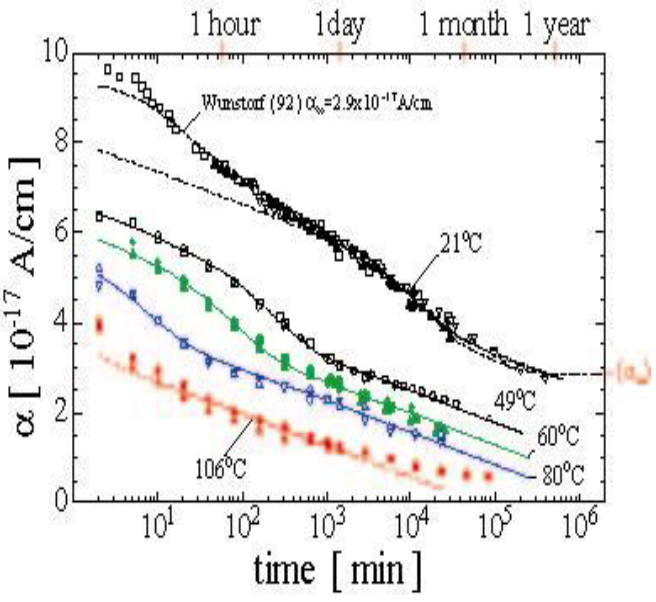

Fig. 11b Damage constant as a function of time, showing initial annealing (Rose Collab)

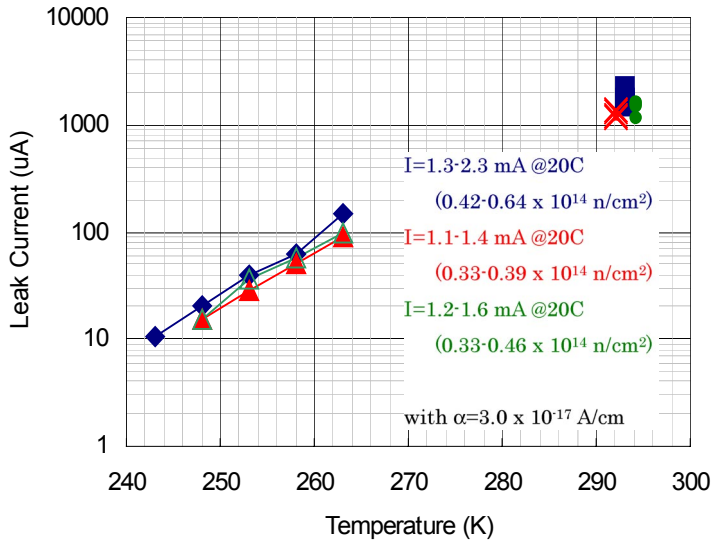

Fig. 11c Leakage current at full depletion and its extrapolation to 20°C. The extrapolation is done for three sets of data described in the text (marks at 20°C are slightly shifted so that difference can be seen).

Extrapolation to 20°C is made using

$$I(T) \propto T^n \exp\left(-E_g / 2k_B T\right)$$

where E_g =1.12eV and n is taken to be 2. The results are barely sensitive to a choice of n=1.5. There are three sets of data plotted in the figure: one set (green) for 001 Sensor and two sets (blue and red) for 002 measured on 45 days and 51 days after irradiation. The range of leakage current thus obtained is 1.1 to 2.3 mA at 20°C. The neutron fluence calculated from these values is 0.33-0.64×10^{14}/cm^2. The present result prefers somewhat smaller neutron fluence but is in reasonable agreement with the anticipated fluence of 0.7×10^{14}/cm^2.

6.2 Full Depletion Voltage

Figure 12a shows C-V curves measured at temperatures at between –25 and –10°C. The LCR frequency was set to 100 Hz. The data are shown for the two sensors. The full depletion voltage obtainable from these curves apparently depends on temperature, which should not be physical. The frequency was chosen so that the C-V curve at lower bias is significant. The frequency dependence is studied at –10 and –20 °C (Fig. 12b). It seems C-V curves measured at higher frequencies (400Hz and 1 kHz) result smaller "full depletion voltage". The determination is,

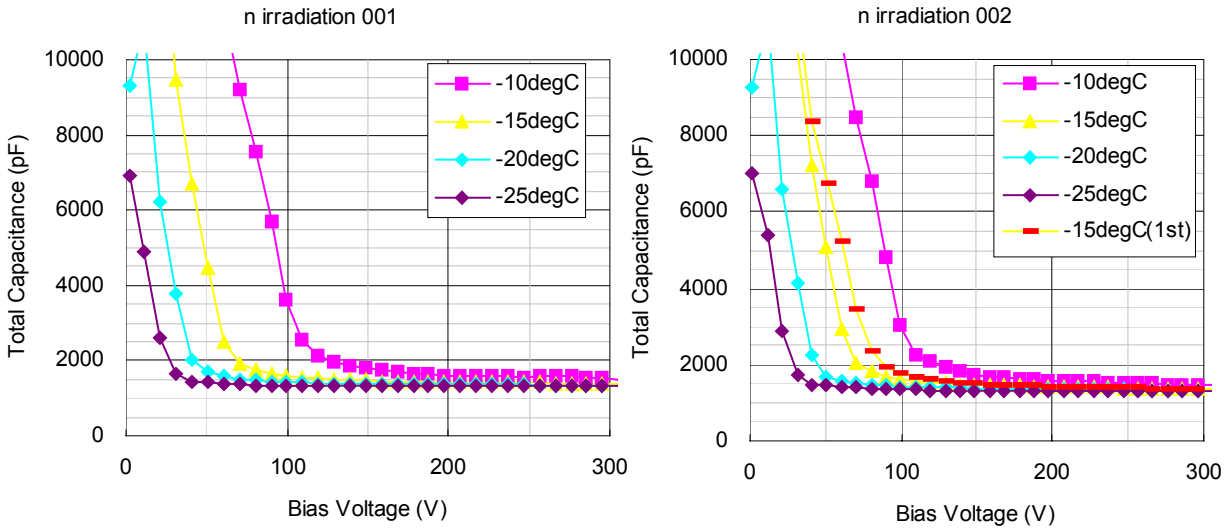

Fig. 12a C-V curves of n-irradiated sample. (Left) 001 Sensor and (Right) 002 Sensor. The data for 002 Sensor are taken 51 days after irradiation and the data on 45 days after are shown for comparison.

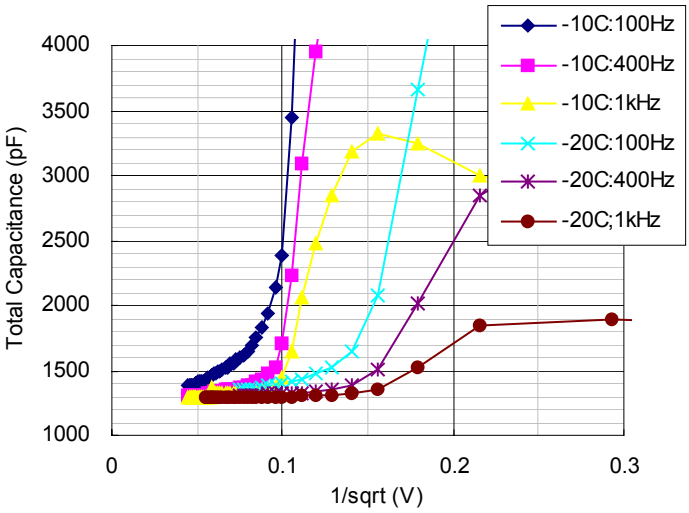

Fig. 12b Frequency dependence of bulk capacitance measured at –10 and –20°C.

however, not straightforward, since we can not perform reliable fits for such data.

The evolution of the full depletion voltage is calculated (see Fig. 12c) using the parameters given by ROSE Collaboration. In the present calculation, we assume that the initial full depletion voltage is 150 V and the sensor is irradiated to equivalent neutron fluence of 0.7×10^{14} /cm^2. Appendix summarizes the equations and the parameters we used, where an expectation for 1.4×10^{14} /cm^2 is also given.

We expect that the full depletion voltage be around 40 V. The C-V measurement should be affected largely by leakage current, and we consider the measurement at lower temperatures represents the intrinsic depletion voltage, which is around 30-40V and is in good agreement with the expectation.

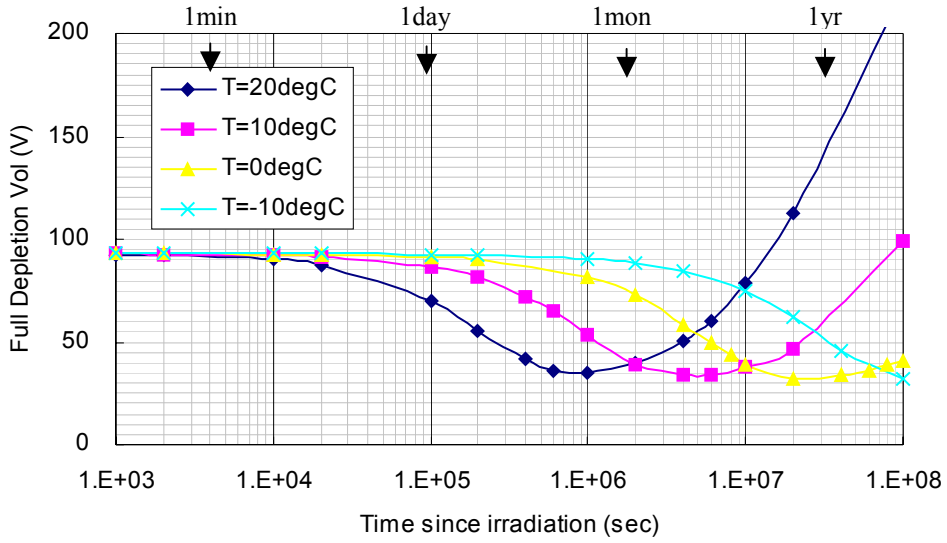

Fig. 12c Evolution of full depletion voltage since completion of irradiation. Parameters are taken from ROSE Collaboration. Initial full depletion voltage 150V, and neutron fluence 0.7×10^{14} /cm^2.

6.3 Interstrip Resistance

The interstrip resistance is one of the key parameters to evaluate the radiation effect on silicon detectors. The oxide layer between strips accumulates positive charges created due to radiation, which degrades the interstrip resistance.

Figure 13 shows bias dependence of the resistance. The data are shown for different temperatures (Sensor 001) and for five sampled strips (Sensor 002) measured at –25°C. The strip leakage current was almost constant to 85-90nA during these measurements. The resistance was greater than 40 GΩ (see Fig. 6) before irradiation. The resistance can be more than 1G Ω if the bias is set at 250V (50V) at –10°C (–25°C). Although the bias voltage 250V is larger than the full depletion voltage, where we naively expect that the strips are isolated, the required voltage is small enough and manageable.

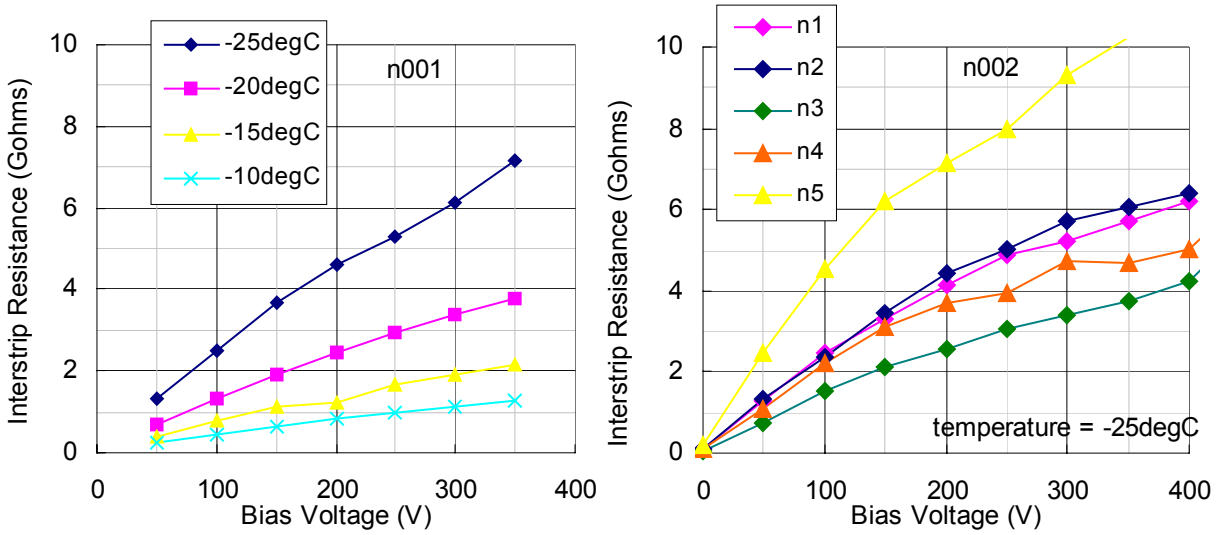

Fig. 13 Interstrip resistance as a function of bias voltage. (Left) Temperature dependence measured for 001 Sensor. (Right) channel dependence measured for 002 Sensor.

6.4 Interstrip Capacitance

The interstrip capacitance of irradiated sensors was measured for sampled strips. Figure 14a shows the bias dependence and LCR frequency dependence measured for a particular set of

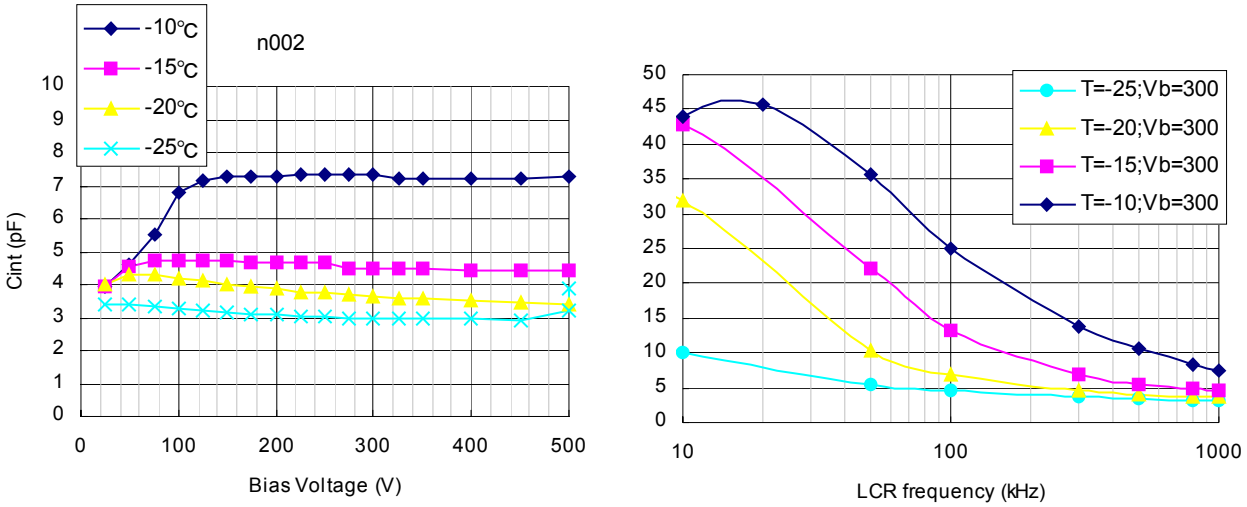

Fig. 14a Interstrip capacitance of irradiated sensor. (Left) Bias dependence measured at LCR frequency of 1MHz, (Right) LCR frequency dependence measured at Vb=300V.

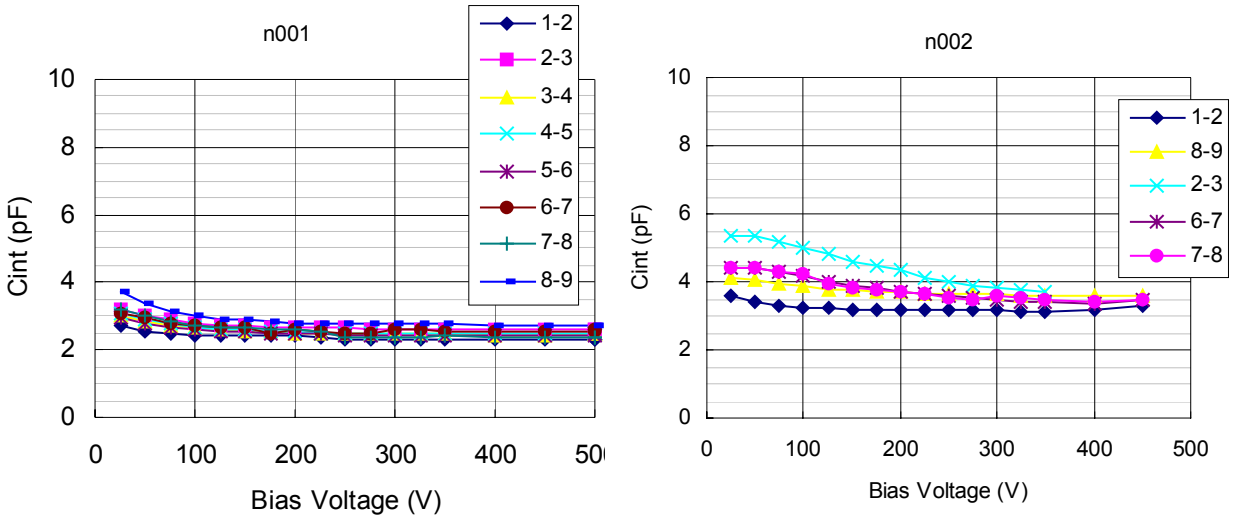

Fig. 14b Interstrip capacitance for sampled strips of (Left) Sensor 001 and (Right) Sensor 002. The LCR frequency is 1MHz and temperature is –25°C.

neighboring strips. The measurements at 1 MHz are affected largely by leakage current, and the measured capacitances are substantially large at higher temperatures. From the frequency dependence, 1MHz is no high enough especially at higher temperatures. It seems all the data approach to 3 pF at higher frequency, the asymptotic value being consistent with that of non-irradiated sensors.

Comparison of different strip pairs is shown in Fig. 14b for the two sensors. The capacitance was measured at –25°C and for 1 MHz LCR frequency. The *p*+ strips are in the ohmic contact side after the bulk is inverted to *p* type. In this case we would expect that the strips are not well isolated unless the bulk is fully depleted. Then, the interstrip capacitance should decrease rapidly around the voltage cross the full depletion voltage. Although it is not very clear from the present data, the decrease is moderate and it requires a voltage of >200V to reach the asymptotic value. This can be explained qualitatively by the positive charges trapped in the oxide layer. The positive charges attract electrons, which depletes partially the *p* bulk in the interstrip region, achieving partial isolation even at small bias (Cint decreases moderately). Also, the electric field in the interstrip region is disturbed by these extra charges, resulting the isolation is not complete even above the full depletion voltage.

7. Mechanical Precisions

We used a Mitutoyo MF-UA measuring microscope to evaluated the mechanical precisions. The reproducibility is about 2 μm horizontally and 3 μm vertically. The vertical position is obtained by focusing.

7.1 Wafer thickness

The wafer thickness was measured for 24 sensors at the center of shorter sides. The sensors were placed vertically under the microscope on the stage. The distribution of 48 measurement results is shown in Fig. 15a. The central value is 320 μm with a spread of about 5 μm. Since we used wafers of the same lot, the spread may become wider at production.

The thickness difference at the two sides of the same sensor was at maximum 5 μm.

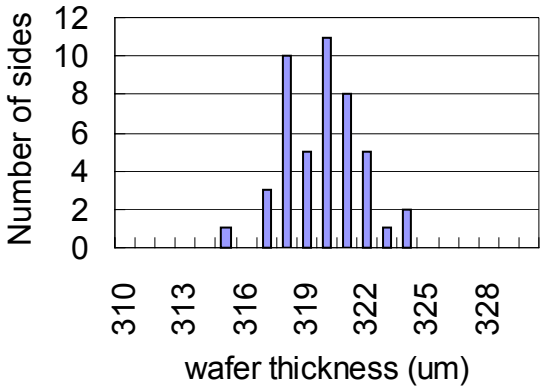

Fig. 15a Wafer thickness distribution

7.2 Edge Cut Precision

The distance between the fiducial mark to the edge was measured at the four corners. The nominal distance is 330 μm. Although no systematic difference between axial and stereo sensors was seen, there are some systematic deviations among the different sides. The right side (the shorter side and hybrid side) tends to be wider than the nominal distance while the left side (the opposite shorter side) tends to be narrower. The systematic difference at the longer sides is

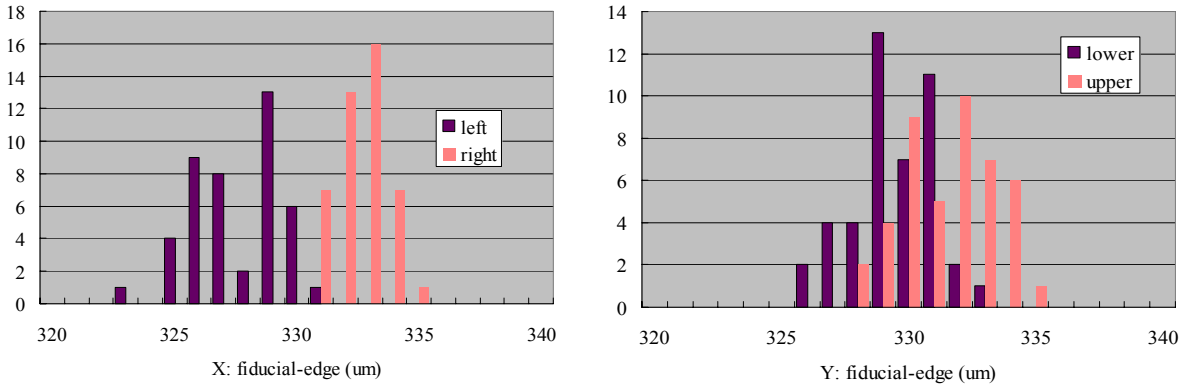

Fig. 15b Distance between the fiducial to the edge.

smaller. The edge cutting for the present samples is precise to 5 μm.

7.3 Sensor Planarity

The sensors tend to be bowed due to the difference in CTEs between SiO_2 and Si: They are flat when processed at high temperature. The bow is more significant for single-sided sensors than for double-sided sensors.

The general profile is measured on 1 cm grids with a laser system at first. Typical results are given in Fig. 15c, where the three corner data are used to define the reference plane and the deviations are plotted. The positive deviations mean that the sensor is bowed with the strip side up. The profile is generally universal among the different sensors.

The height at the sensor center was measured with a microscope together with the heights at the fiducials when the edge cut precision data were taken. The height relative to the fiducial heights is histogrammed in Fig. 15d. The warp is typically 80 to 100 μm for axial sensors, while it is 55 to 90 μm for stereo sensors. The difference could be partially explained by that the stereo sensors are wider then axial sensors.

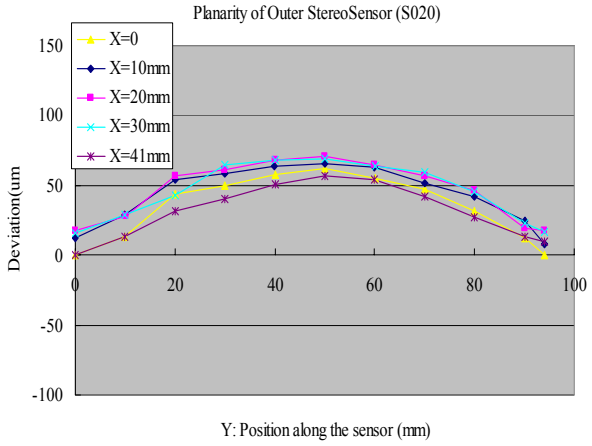

Fig. 15c Typical Z profile of a stereo sensor

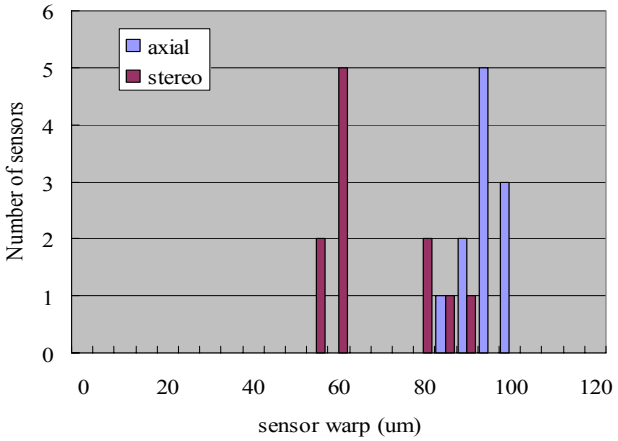

Fig. 15d The deviation in Z at the sensor center

8. Conclusions

We have evaluated the electrical performance of axial and stereo prototypes fabricated for the SVX2b detector. The prototypes fulfill our specifications. The leakage current is small and most sensors show no breakdown up to 1000V, our specification being 500V. Number of dead channels is quite small. We fully understood the faulty strips reported by the manufacturer. In addition, we found some new faulty strips. New punch-throughs are due to a parameter miss-understanding at testing of axial sensors. We have found no new punch-through for stereo sensors. We recognized a limitation in detecting readout implant opens by HPK: We found five new readout implant opens out of in total 36 tested sensors (out of more than 18k strips).

Two sensors irradiated with neutrons are characterized. The measurement results of I-V, C-V, interstrip capacitance and resistance, and polysilicon resistance are consistent with characteristics previously known. The expected full depletion voltage after 0.7×10^{14} n/cm^2 is about 40 V, our data being consistent with this expectation. Because of bulk type inversion and large leakage current, we require a bias of typically 200V, much higher than the full depletion voltage, to achieve good isolation between strips and to minimize the interstrip capacitance.

The mechanical precisions have been measured, which are satisfactory for our application.

Appendix. Equations used to calculate evolution of full depletion voltage

The full depletion voltage of silicon sensor with thickness of d is given by

$$V_{FD} = \frac{|N_{eff}|ed^2}{2\varepsilon}$$

under planer diode assumption. Here permittivity of silicon is $\varepsilon = 11.9 \times 8.85 \times 10^{-14}$ F/cm. The same equation is used to calculate the initial impurity density $N_{eff\,0}$ using the initial full depletion voltage (150 V).

The initial n type impurity density decreases with radiation (and time) since new levels of displacement damages induced by radiation act as effectively p type:

$$N_{eff} = N_{eff\,0} - N_{damage}(\phi, t, T)$$

The radiation effects can be classified into three types.

$$N_{damage}(\phi, t, T) = N_c(\phi) + N_a(\phi, t, T) + N_Y(\phi, t, T)$$

The first effect is stable damage, representing increase of donor type impurities and creation of acceptor type impurities, which is expressed by the following equation:

$$N_c(\phi) = N_{c0}\left(1 - \exp(-c\phi)\right) + g_c\phi$$

The fraction N_{c0} / N_c refers to "incompleteness" in donor removal.

The second effect is short-term annealing after irradiation.

$$N_a(\phi, t, T) = g_a\phi \exp\left(-k_{a0}t \exp\left(-E_{aa} / k_B T\right)\right)$$

where the model assumes activation energy E_{aa} and time constant k_{a0}.

The last effect is long-term reverse annealing:

$$N_Y(\phi, t, T) = g_Y\phi\left(1 - \frac{1}{1 + k_{Y10}t \exp(-E_{aY} / k_B T)}\right)$$

The parameters used in the calculation are listed below.

$N_{c0} = 0.65 N_{eff\,0}$

$c = 1.1 \times 10^{-13}$ cm^2

$g_c = 1.49 \times 10^{-2}$ cm^{-1}

$g_a = 1.81 \times 10^{-2}$ cm^{-1}

$g_Y = 5.16 \times 10^{-2}$ cm^{-1}

$k_{a0} = 2.4 \times 10^{13}$ s^{-1}

$k_{Y10} = 1.5 \times 10^{15}$ s^{-1}

$E_{aa} = 1.09$ eV

$E_{aY} = 1.33$ eV

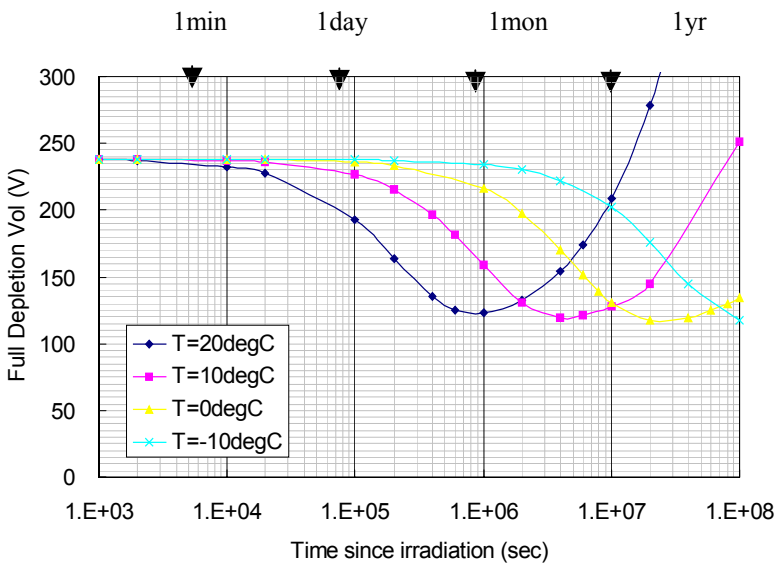

Similar to Fig. 11e, but for neutron fluence 1.4×10^{14} /cm^2